Supporting Information

Low-Loss Anisotropic Image Polaritons in van der Waals Crystal α-MoO$_3$

Sergey G. Menabde, Junghoon Jahng, Sergejs Boroviks, Jongtae Ahn, Jacob T. Heiden, Do Kyung Hwang, Eun Sung Lee, N. Asger Mortensen, and Min Seok Jang*

Supporting Information

Low-loss anisotropic image polaritons in van der Waals crystal α-MoO₃

Sergey G. Menabde, Junghoon Jahng, Sergejs Boroviks, Jongtae Ahn, Jacob T. Heiden, Do Kyung Hwang, Eun Sung Lee, N. Asger Mortensen, and Min Seok Jang[*]

S1. Fourier analysis of the near-field interference fringes

In general, near-field signal over the gold substrate at mid-infrared frequencies has very high signal-to-noise ratio due to the large near-field reflection coefficient. Therefore, analysis of the mid-infrared image modes on gold can be accomplished with higher precision than probing of modes on a dielectric substrate.

We use s-SNOM to map the near-field amplitude over the area of interest. The long straight edges of the gold crystals launch polaritonic waves with a planar wavefront via scattering of the incident excitation beam of the s-SNOM. The diameter of the focused laser spot on the sample is $> \lambda_0 \approx 10$ μm, which is much larger than the image polariton wavelength $\lambda_P \sim 400 - 800$ nm. Therefore, the illumination beam can be considered as quasi-uniform across the area of near-field interference. Hence, the near-field amplitude is proportional to the electric field amplitude of the propagating polaritons.

Analysis of the near-field HIP interference fringes is shown in Fig. S1. In order to take the Fourier transform of the near-field fringes measured by s-SNOM (Fig. S1A), the integrated fringes profile (Fig. S1B; black) is fitted with a polynomial curve (red) corresponding to the near-field background signal, which is then subtracted from the near-field data. The background-free interference fringes (blue) are analyzed by the Fourier transform, and the resulting spectrum (Fig. S1C; grey) is fitted with the Lorentzian profile (red) in a form of a spectrum of the damped cosine function. Thus, the Lorentzian reveals the real part (peak frequency) and the imaginary part (FWHM) of the polariton's complex-valued propagation constant. The double-frequency signal of the tip-launched HIP is also clearly visible (green Lorentzian profile). Similar procedure is applied to the HPP fringes over the glass substrate.
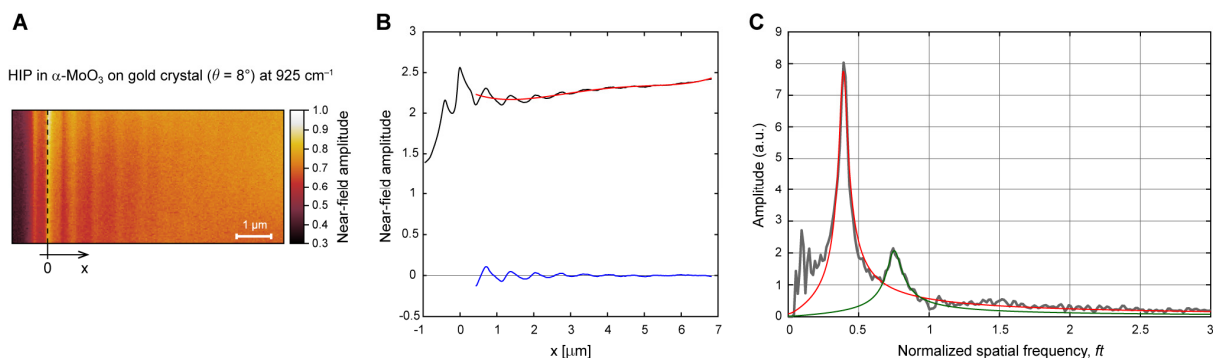
Figure S1. Analysis of near-field interference fringes. (A) Near-field image of the α-MoO₃ on the gold crystal near its edge (indicated by the black dashed line), measured by s-SNOM at the excitation frequency of 925 cm⁻¹ and $\theta = 8°$ at the sample shown in Fig. 1C in the main text; near-field signal is demodulated at third harmonic of the nano-tip oscillation frequency. (B) Profile of the near-field interference fringes integrated over the whole scan area in (A) (black), the background signal polynomial fit (red), and the background-free interference fringes (blue). (C) Fourier spectrum of the background-free fringes (grey) and its Lorentzian fit – the one corresponding to the HIP mode (red) and the double-frequency signal of the tip-launched HIP (green). Spatial frequency is normalized by α-MoO₃ thickness $t = 260$ nm.

S2. Dispersion and damping of HPP modes

We obtained near-field images of the interference fringes at both sides of the gold edge. As we mention in the main text, only the HIP fringes provide an accurate information on the polariton damping in α-MoO₃ since the only significant loss channel in this case is the material loss. The HPP suffers from the additional loss in glass substrate which is lossy at the frequencies of interest. However, as can be seen in Fig. 1D in the main text, gold flakes of finite thickness (typically 0.1-0.5 μm) cause the α-MoO₃ to be suspended immediately next to the gold edge. Therefore, the dispersion of HPP in our samples is expected to be very close to that of the HPP in a free-standing waveguide.

Figure S2 demonstrates the dispersion of HPP at the same frequencies and angles as the HIP (Fig. 3A in the main text). Indeed, at most angles, measured dispersion (red circles) well agrees with the theoretical one calculated for the free-standing slab (color map). Figure S2 shows measurement results only by s-SNOM; the PiFM scans did not reveal the HPP fringes.

We also analyzed the FOM and the lifetime of HPP obtained from the near-field interference of the edge-launched modes. Polariton lifetime is calculated as $\tau \approx L/v_g$, where $L = 1/k_P''$ is the propagation length and $v_g = \partial\omega/\partial k_P$ is the group velocity. Since the measured HPP dispersion well agrees with that in a free-standing waveguide, the latter case is used to analytically calculate the group velocity. Figure S3A shows the FOM data, and Figs. S3B and C show the lifetime in the corresponding Reststrahlen bands.

As evident from the lifetime in RB2 and RB3, the experimentally measured values correspond to the HPP in a partially suspended α-MoO₃ which is still affected by the presence of lossy glass substrate underneath.

This is particularly evident from the difference between the data in RB2 and RB3: lifetime of the more confined HPP in RB3 tend to agree with the prediction for the free-standing case, while the less confined HPP at lower frequencies in RB2 has its lifetime approaching the free-standing values.
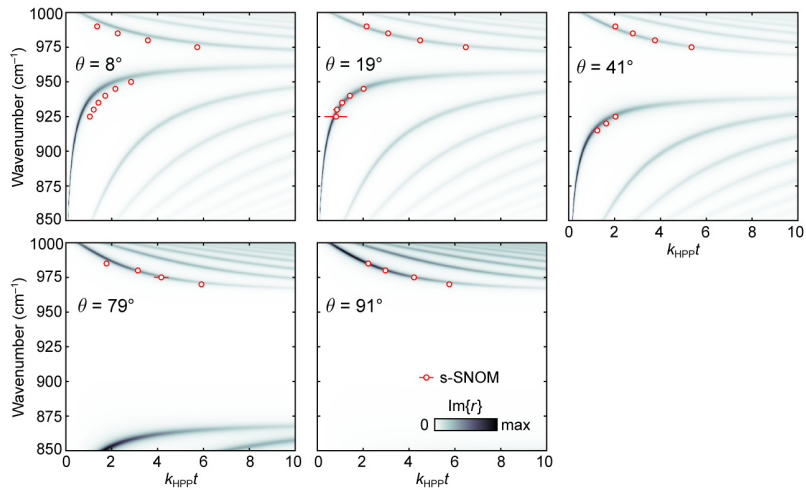

Figure S2. HPP dispersion. The experimentally extracted data (red circles) measured in our samples and the numerically calculated HPP dispersion in a free-standing α-MoO₃ (color map). Particularly good match between the theoretical and experimental data at θ = 19°, 41°, and 79° indicates the presence of a significant air gap between the α-MoO₃ and glass substrate in this particular sample, also visible in its optical image (Fig. 1D in the main text).
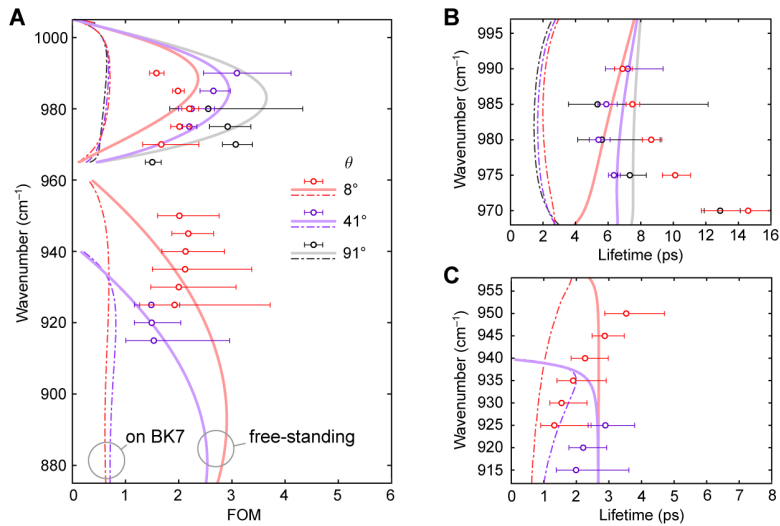

Figure S3. FOM and lifetime of HPP. (A) Measured (circles) and analytically calculated (curves) FOM of the HPP launched by gold crystal edges with θ = 8°, 41°, and 91°. Calculated data is shown for the free-standing α-MoO₃ (solid curves) and the α-MoO₃ on BK7 glass substrate (dash-dot curves). (B) Lifetime of the HPP in RB3. (C) Lifetime of the HPP in RB2.

S3. Dielectric function of α-MoO₃

Dielectric function of α-MoO₃ can be modelled by a system of three Lorentzian oscillators in a general TO-LO form, providing the permittivity for each crystallographic direction:

$$\varepsilon_m(\omega) = \varepsilon_{\infty,m}\left(\frac{\omega_{LO,m}^2 - \omega^2 - i\Gamma_m\omega}{\omega_{TO,m}^2 - \omega^2 - i\Gamma_m\omega}\right), m = x, y, z$$

where ω_{LO}, ω_{TO}, Γ and ε_∞ are the LO and TO phonon frequencies, phonon damping, and the high-frequency permittivity, respectively. The anisotropic permittivity tensor is given by:

$$\bar{\bar{\varepsilon}} = \begin{bmatrix} \varepsilon_x & 0 & 0 \\ 0 & \varepsilon_y & 0 \\ 0 & 0 & \varepsilon_z \end{bmatrix}$$

For the polaritons propagating in the *x-y* plane at angle θ to the *x*-axis, the effective permittivity is given by $\bar{\bar{\varepsilon}}' = U\bar{\bar{\varepsilon}}U^T$, where U is the rotation matrix:

$$U = \begin{pmatrix} \cos\theta & -\sin\theta & 0 \\ \sin\theta & \cos\theta & 0 \\ 0 & 0 & 1 \end{pmatrix}$$

Hence, the in-plane effective permittivity is given by: $\varepsilon_\perp = \varepsilon_x\cos^2\theta + \varepsilon_y\sin^2\theta$.

First, we fitted the collected experimental data for HIP (at all angles and frequencies shown in Fig. 3A in the main text) with the corresponding dispersion curves given by Equation (1) in the main text. Then we used the measured values of FOM to adjust Γ based on the calculated FOM from the dispersion Equation (1). Fitted parameters of the dielectric function are shown below in the Table S1, along with previously reported data, which shows a good agreement.

	This work				Ref. [S1]				Ref. [S2]			
	ω_{TO}	ω_{LO}	Γ	ε_∞	ω_{TO}	ω_{LO}	Γ	ε_∞	ω_{TO}	ω_{LO}	Γ	ε_∞
									506.7	534.3	49.1	
x	820	965.6	4	7.56	820	972	4	4.0	821.4	963.0	6.0	5.78
									998.7	999.2	0.35	
y	545	851	4	7.85	545	851	4	5.2	544.6	850.1	9.5	6.07
z	964	1005.1	1.3	2.51	958	1004	2	2.4	956.7	1006.9	1.5	4.47

Table S1. Recovered parameters of the α-MoO₃ dielectric function.

S4. Surface roughness of monocrystalline gold and exfoliated α-MoO$_3$

Figure S4 shows the high-resolution AFM scans of surface topography of the typical monocrystalline gold and the exfoliated α-MoO$_3$ flakes. Both surfaces have RMS roughness of ≈ 150 pm. Such a smooth interfaces in the samples assure the scattering-free propagation of polaritons.
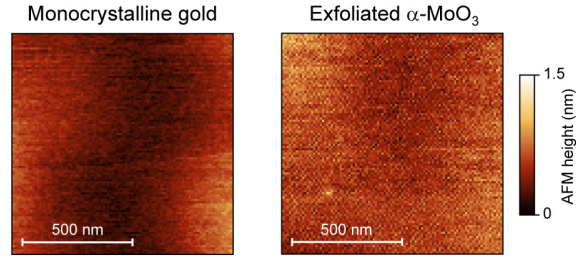

Figure S4. AFM-measured surface topography of the monocrystalline gold and exfoliated α-MoO$_3$ flake, having similarly smooth surfaces with RMS roughness of ~1 Å. RMS roughness of both surfaces is ≈ 150 pm.

S5. Analysis of the flakes bending over the gold edges

Thin (100-300 nm-thick) α-MoO$_3$ flakes inevitably bend over the edge of the gold crystals which have typical height of 200-500 nm. Figure S5 shows the surface topography (top panels, in gray-scale) of α-MoO$_3$ and the corresponding near-field phase map (bottom panels) from the same SNOM measurements of three different samples. Near-field phase reveals the position of the gold edge under the α-MoO$_3$ where the abrupt change of the near-field scattering coefficient causes the sharp change of the near-field phase (indicated by the dashed gray line). The red curve shows the AFM height measured relative to the lowest point of each scan. As indicated in Fig. S5, the bending of α-MoO$_3$ on top the gold crystal does not exceed ≈ 5 nm of height per several micrometers of length. Such a small surface curvature can be safely considered adiabatic for the propagating HIP in our system, and thus does not introduce any significant scattering.

At the same time, material bending implies that a non-zero air gap is formed between the gold and α-MoO$_3$. Considering the constant thickness of our α-MoO$_3$ flakes, we assume the maximum air gap thickness is given by the AFM surface profile, as shown in Fig. S5. The maximum air gap of 5.5 nm is expected for the thinnest α-MoO$_3$ flake with thickness t = 172 nm (Fig. S5B). In order to confirm that the air gap does not distort the HIP dispersion, we calculated the complex propagation constant of HIP in the presence of the air gap for the worst-case scenario (5.5 nm gap and t = 172 nm). Dispersion and FOM of HIP in the presence of air gap are shown in Fig. S6. Our calculations indicate that the dispersion of HIP is affected only near the TO frequency in the RB2 (Fig. S6A), while the FOM (i.e. propagation loss) is practically insensitive to the presence of the gap (Fig. S6B). Since the possible gap size is even smaller under the thicker samples, and considering that the experimental data agrees with the material model equally well for all samples, we conclude that our analysis is not significantly affected by the possible presence of the air gap.
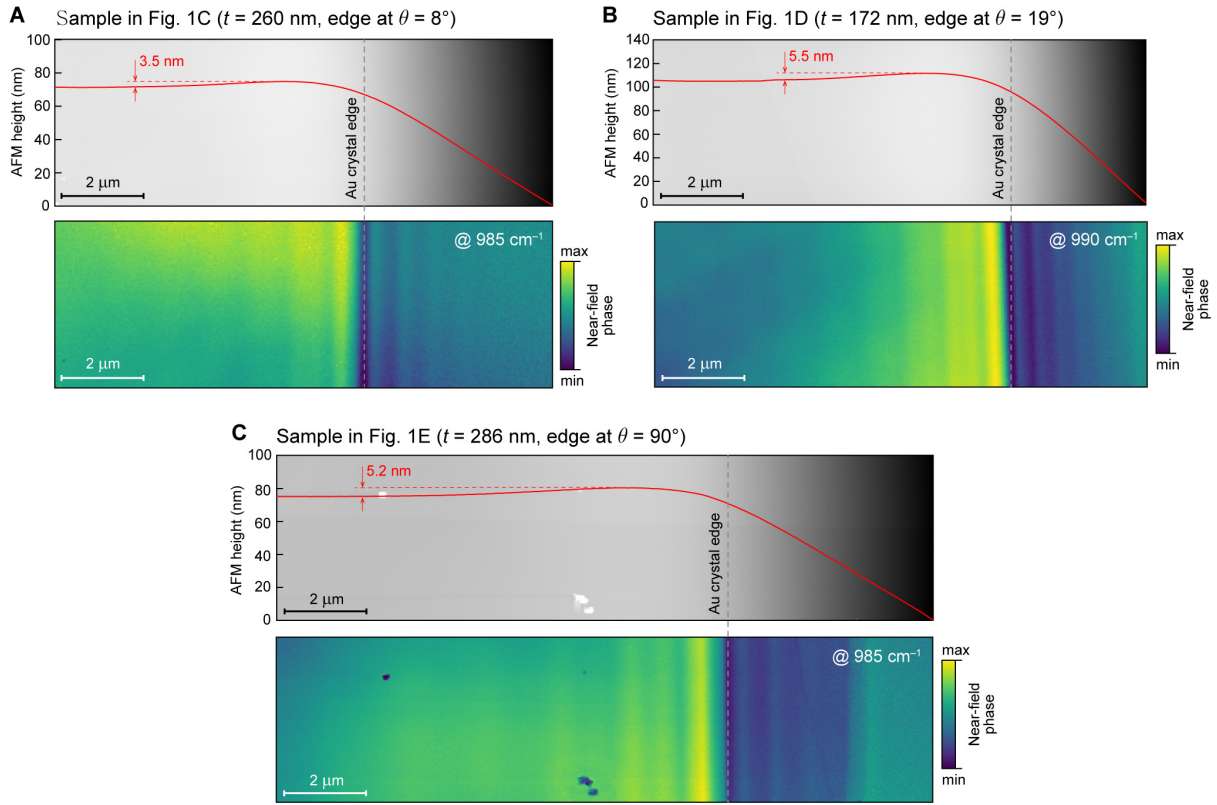
Figure S5. AFM data from SNOM. Surface topography (top panels) and the corresponding near-field phase map (bottom panels) of the α-MoO₃ flakes on the monocrystalline gold near the gold edge. All panels are shown in same scale. Red curve shows the AFM height relative to the lowest measured point. Dashed line indicates the position of the gold crystal edge under the α-MoO₃ flake revealed by the abrupt change of the near-field scattering coefficient.
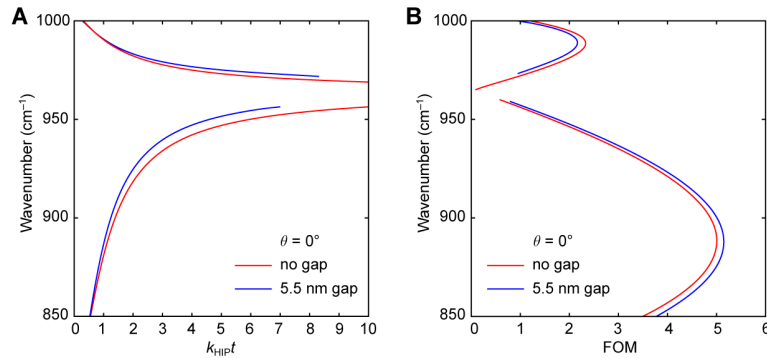

Figure S6. Effect of the air gap on the HIP dispersion. (A) Analytically calculated dispersion and (B) FOM of the HIP modes with and without the 5.5 nm-thick air gap between the gold and the α-MoO₃ flake of thickness 172 nm.

The dispersion of the four-layer uniform structure BK7/air/α-MoO₃/air is calculated by searching for the system's eigenmodes using the transfer matrix formalism [S3]. This semi-analytical method provides the accurate value of the complex propagation constant of the propagating eigenmodes supported by a given multilayer system. At the same time, the polaritonic dispersion in the three-layer structure considered in the

main text (without the air gap) is well-approximated by the dispersion Equation (1), derived under the high-momentum approximation for mid-IR phonon-polaritons in thin wan der Waals crystals [S4].

References

[S1] Z. B. Zheng, N. S. Xu, S. L. Oscurato, M. Tamagnone, F. S. Sun, Y. Z. Jiang, Y. L. Ke, J. N. Chen, W. C. Huang, W. L. Wilson, A. Ambrosio, S. Z. Deng, H. J. Chen, *Sci. Adv.* **2019**, *5*, eaav8690.

[S2] G. Alvarez-Perez, T. G. Foland, I. Errea, J. Taboada-Gutierrez, J. H. Duan, J. Martin-Sanchez, A. I. F. Tresguerres-Mata, J. R. Matson, A. Bylinkin, M. Z. He, W. L. Ma, Q. L. Bao, J. I. Martin, J. D. Caldwell, A. Y. Nikitin, P. Alonso-Gonzalez, *Adv. Mater.* **2020**, *32*, 1908176.

[S3] S. G. Menabde, I. H. Lee, S. Lee, H. Ha, J. T. Heiden, D. Yoo, T. T. Kim, T. Low, Y. H. Lee, S. H. Oh, M. S. Jang, *Nat. Commun.* **2021**, *12*, 938.

[S4] G. Alvarez-Perez, K. V. Voronin, V. S. Volkov, P. Alonso-Gonzalez, A. Y. Nikitin, *Phys. Rev. B* **2019**, *100*, 235408.